Pore-resolved simulations of ammonia combustion in porous inert media

R. Puri[1*], T. Zirwes[2], O. T. Stein[1]

*rishabh.puri@kit.edu

[1] *KIT - Karlsruhe Institute of Technology, Engler-Bunte-Institute, Simulation of Reacting Thermo-Fluid Systems, Engler-Bunte Ring 7, D-76131 Karlsruhe, Germany*

[2] *University of Stuttgart, Institute for Reactive Flows, Pfaffenwaldring 31, D-70569 Stuttgart, Germany*

Abstract

Liquid ammonia is considered to be a suitable hydrogen carrier for a future carbon-free energy infrastructure, but NH_3 can also be used as a fuel for direct combustion. However, NH_3 exhibits poor combustion characteristics in conventional burners due to its low heating value, difficult flame stabilisation, and comparatively high pollutant emissions. Porous media combustion (PMC) is utilised in this work to improve the combustion characteristics of ammonia. In a first step, parameter studies through volume-averaged simulations (VAS) are conducted to pre-select suitable burner configurations and operating conditions. This narrows down the range of suitable configurations for effective flame stabilisation and low NO_x formation. Then, direct pore-level simulations (DPLS) of these geometries are performed. Flame propagation and stabilisation in the DPLS are influenced by the foam surface temperature, geometry and local acceleration of the flow. Ammonia dehydrogenation leads to H_2 production, but has minimal effect on the combustion characteristics. DPLS results show considerable discrepancies with VAS due to the simplified modelling of the porous structure in VAS and the absence of heat conduction in the solid in the present DPLS.

Introduction

Hydrogen and hydrogen-based fuels are poised to be essential for a net zero-carbon energy economy [1, 2]. Ammonia is a carrier of hydrogen and can be decomposed to generate molecular hydrogen [3]. Furthermore, NH_3 can be stored and transported using the existing infrastructure, thus providing a potential storage solution for H_2 as a fuel [4]. Direct combustion of ammonia is attractive for power generation and industrial applications [5, 6], but combustion of NH_3 has its own challenges. Ammonia exhibits fuel toxicity, low flame stability and high levels of nitrogen oxide emissions [7].

In this work, these challenges are addressed by utilising Porous Media Combustion (PMC) [8, 9]. PMC is defined as the combustion of a fuel/oxidiser mixture within a solid matrix. The flame burns inside the pores and heat is re-circulated from the downstream post-flame region to the upstream reactant mixture through conduction and solid-to-solid radiation. The heat transfer within the solid matrix and heat re-circulation towards the upstream fuel/oxidiser mixture can improve the stability of NH_3/air flames. The physics governing PMC are an interplay of flow dispersion within the solid matrix, complex chemical kinetics, conjugate, and radiative heat transfer [10]. These physical phenomena can be investigated in detail numerically by performing direct pore-level simulations (DPLS). In this way, detailed transport models and complex chemical kinetics are considered for the gas phase, which can then be coupled to a resolved solid structure. DPLS of PMC are computationally intensive and often performed in 2D or by only resolving the gas phase [11, 12]. DPLS of steady-state combustion of CH_4/air in cylindrical and radial burners were performed by Bedoya et al. [13]. The porous structure was obtained using computed tomography and single-step chemistry was used. Fergusen et al. [11] investigated conjugate heat transfer (CHT) in pore-resolved 2D simulations of lean methane/air PMC. Flame stability was found to be influenced by preheating, which in turn depended on the solid conductivity. Liu et al. [14] performed 2D pore-level simulations of CH_4/air combustion in a two-layer porous burner. Surface radiation in the solid

matrix was also considered. The authors investigated the influence of inlet velocity and solid thermal conductivity on inter-phase thermal non-equilibrium and the largest temperature difference between the phases was observed in the combustion zone near the flame front. The specific surface area of the porous structure was also found to be a defining factor influencing the radiation efficiency of two-zone porous radiant burners investigated through DPLS [15]. Recently, Muller et al. [16] analysed the anchoring mechanisms and the burning rate enhancement for lean hydrogen/air flames embedded in inert porous media. DPLS were performed with detailed chemical kinetics. Preferential diffusion was observed to have a major effect on flame stabilisation and burning rate.

Given the high computational cost of DPLS, volume-averaged simulations (VAS) have been widely utilised for PMC simulations [17–19]. This volume-averaged approach for PMC is also described in literature with the term volume-averaged model (VAM), but the term VAS is used in the present work. VAS are reduced and thus computationally cost-efficient models, where the gas and solid phases are not individually resolved. The effects of flow dispersion, conjugate, radiative, and inter-phase heat transfer are modelled using the effective properties of the porous structure. Suitability of VAS has been evaluated against experimental data and DPLS [13, 19, 20]. Zirwes et al. [21] developed a 1D-VAS-framework within Cantera [22] for simulating NH_3-H_2-air combustion in a multi-layer porous burner. The effective material properties were obtained from X-ray micro-computed-tomography (μ-CT) scans and thermal simulations of the porous structure. The VAS had better congruence with measurements when effective material properties were calculated from well-defined geometries and first-principle methods instead of empirical correlations.

In the present work DPLS are performed for NH_3/air combustion in a single layer porous burner. VAS are used to predict emissions from the porous burner for various operating conditions in a new simulation framework based on OpenFOAM. A burner operating condition with low emissions is used for DPLS. The governing equations and the numerical approach of DPLS as well as the corresponding VAS are explained in the following sections. This is followed by a discussion of the DPLS results and a comparison of the DPLS and VAS predictions.

Direct pore-level simulations

Governing equations

The OpenFOAM-based transient reacting flow solver EBIdnsFoam [23] is used for performing the DPLS. The governing equations are

$$\frac{\partial \rho}{\partial t} + \nabla \cdot (\rho \vec{u}) = 0 \tag{1}$$

$$\frac{\partial (\rho \vec{u})}{\partial t} + \nabla \cdot (\rho \vec{u}\vec{u}) = -\nabla p + \nabla \cdot \boldsymbol{\tau} + \rho \vec{g}, \qquad \boldsymbol{\tau} = \mu \left(\nabla \vec{u} + (\nabla \vec{u})^T - \frac{2}{3}\mathbf{I} \nabla \cdot \vec{u} \right) \tag{2}$$

$$\frac{\partial (\rho h_{\mathrm{tot}})}{\partial t} + \nabla \cdot (\rho \vec{u} h_{\mathrm{tot}}) = -\nabla \cdot \vec{q} + \frac{\partial p}{\partial t} - \sum_i (h_i^o \dot{\omega}_i) \tag{3}$$

$$\vec{q} = \sum_k h_{\mathrm{sens},k} \left(\vec{j}_k - Y_k \sum_k \vec{j}_k \right) + \frac{\lambda}{c_p} \left(\sum_k h_{\mathrm{sens},k} \nabla Y_k - \nabla h_{\mathrm{sens}} \right) \tag{4}$$

$$\frac{\partial (\rho Y_k)}{\partial t} + \nabla \cdot (\rho (\vec{u} + \vec{u}_c) Y_k) = \dot{\omega}_k - \nabla \cdot \vec{j}_k, \qquad \vec{u}_c = -\frac{1}{\rho} \sum_i \vec{j}_i \tag{5}$$

where $\vec{u}$ is the velocity, ρ the density, p the pressure, $\vec{g}$ the gravitational acceleration, $\mathbf{I}$ the identity tensor, λ the heat conductivity of the gas mixture, c_p the isobaric heat capacity, Y_k the mass fraction of species k and $\dot{\omega}_k$ its reaction rate. The total sensible energy is $h_{tot} = h_{sens} + 0.5(\vec{u} \cdot \vec{u})$, with the sensible enthalpy h_{sens} and the enthalpy of formation h_k^o of species k. The diffusive species fluxes $\vec{j}_k$ are calculated using the Hirschfelder-Curtiss [24] approximation. The above set of partial differential equations is closed by the ideal gas law. The solver is coupled with the open-source chemistry library Cantera [22] to calculate transport properties and chemical source terms. The external solver SUNDIALS [25] is used to solve the ordinary differential equations for computing chemical source terms.

Computational setup

A 8×8 mm section of the burner with a surface load of 0.25 MW/m^2 is used to define the computational grid for the DPLS, see Fig. 1 (left). The burner axis is aligned with the x-direction and symmetry boundary conditions are used in y- and z-directions. The perforated plate at the burner inlet, upstream of the porous zone, is not resolved. Instead, the inlet is defined with symmetric channels of length 25 mm, each having a diameter of 1 mm. For the selected burner power setting, the incoming mass flux of the NH_3/air mixture for $\phi = 0.9$ is 2.6 kg/m^2, which leads to an inlet velocity of 2.42 m/s. The temperature at the channel inlet is 300 K and linearly increases to 1430 K at the channel exit, i.e. at the base of the porous medium. The temperature of the burner base between the channels is fixed at 1430 K.

The ceramic porous material has an industrial designation of 15 PPI (pores per inch) and its geometry is extracted from µ-CT scans (see Fig. 2) performed on a CT-ALPHA X-ray scanner (ProCon X-ray, Germany) with a Dexela Type 1512 (Perkin Elmer, Germany) detector at TU Freiberg, Germany. The operating parameters for µ-CT are summarised in Tab. 1. The grid is generated using the `snappyHexMesh` tool available with OpenFOAM and the porous zone is refined such that the cell size (4×10^{-5} m) is smaller than one tenth of the thickness of a freely propagating flame (6×10^{-4} m) calculated for the same operating conditions. The computational grid in the channels and the porous zone is shown in Fig. 1 (right). The gas phase is fully resolved, and the effect of heat transfer between the gas and solid phases is implemented as a temperature boundary condition (extracted from VAS) on the surface of the ceramic foam. The zone downstream of the porous medium consists of completely burnt gas, where the cell size is 3.5×10^{-4} m. The downstream gas phase ensures uniform species distributions at the burner outlet. The computational domain has a total of 12 million grid cells.

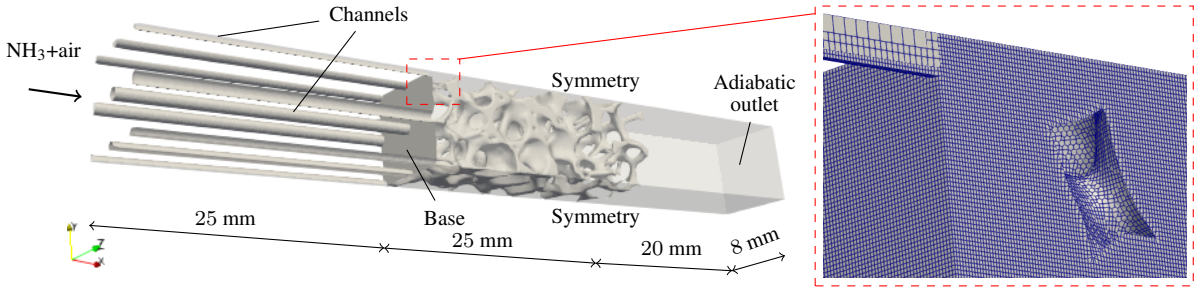

Figure 1. Computational domain of the single-layer porous burner (left). Local mesh refinement in the porous zone (right).

Table 1. Parameters from X-ray µ-CT.

Parameter (unit)	Value
X-ray voltage (kV)	150
X-ray current (µA)	70
Voxel size (µm)	39
Scan size (voxels)	1600×1380×624

A fourth-order interpolation scheme is used for the spatial derivatives. Time integration is performed using the Crank-Nicholson scheme and the transient simulations are conducted with a maximum CFL number of 0.3. Detailed chemistry is calculated using the NH_3/air mechanism developed by Stagni et al. [26]. The DPLS are performed on the CPU partition of the JUWELS supercomputer at the Jülich Supercomputing Center (JSC). Each node is equipped with two Intel Xeon Platinum 8168 CPUs with 48 cores clocked at 2.7 *GHz*. A total of 63 nodes (3,024 cores) is used for running the parallel DPLS which requires approximately 360,000 CPU-h until convergence.

Volume-averaged simulations

Governing equations

The 3D reacting flow solver is used as the basis for the VAS model. The governing equations are written for volume-averaged variables $\bar{\bar{\theta}}$ defined as

$$\bar{\bar{\theta}}_g = \frac{1}{\mathcal{V}_g}\int_{\mathcal{V}_g} \theta \,\mathrm{d}V \;\text{ and }\; \bar{\bar{\theta}}_s = \frac{1}{\mathcal{V}_s}\int_{\mathcal{V}_s} \theta \,\mathrm{d}V \tag{6}$$

where the subscripts g and s denote the gas and solid phase, respectively. For simplicity, the variables in the following equations are written without the averaging ($\bar{\bar{}}$) notation and properties without subscript denote the properties of the gas phase. The governing equations for the gas phase consider the effect of porosity, dispersion, tortuosity, conjugate and radiative heat transfer on the combustion process, viz.

$$\frac{\partial(\gamma\rho)}{\partial t} + \nabla\cdot(\gamma\rho\vec{u}) = 0 \tag{7}$$

$$\frac{\partial(\gamma\rho\vec{u})}{\partial t} + \nabla\cdot(\gamma\rho\vec{u}\vec{u}) = -\gamma\nabla p + \nabla\cdot(\gamma\boldsymbol{\tau}) + \gamma\rho\vec{g} - \vec{u}_{\mathrm{sup}}\left(\frac{\mu}{k_1} + \frac{\rho}{k_2}|\vec{u}_{\mathrm{sup}}|\right) \tag{8}$$

$$\frac{\partial(\gamma\rho h_{\mathrm{tot}})}{\partial t} + \nabla\cdot(\gamma\rho\vec{u}h_{\mathrm{tot}}) = -\nabla\cdot(\gamma\vec{\dot{q}}) + \gamma\frac{\partial p}{\partial t} - \gamma\sum_k(h_k^0\dot{\omega}_k) - h_v(T-T_s) \tag{9}$$

$$\vec{\dot{q}} = -\frac{1}{2}\rho|\vec{u}|d_{\mathrm{disp}}\nabla h_{\mathrm{sens}} + \sum_k h_{\mathrm{sens},k}\left(\vec{j}_k - Y_k\sum_i\vec{j}_i\right) + \frac{\lambda}{c_p\eta}\left(-\nabla h_{\mathrm{sens}} + \sum_k h_{\mathrm{sens},k}\nabla Y_k\right) \tag{10}$$

$$\frac{\partial(\gamma\rho Y_k)}{\partial t} + \nabla\cdot(\gamma\rho(\vec{u}+\vec{u}_c)Y_k) = \gamma\dot{\omega}_k - \nabla\cdot(\gamma\vec{j}_k) \tag{11}$$

where γ is the porosity and $\vec{u}_{\mathrm{sup}} = \gamma\vec{u}$ is the superficial velocity. The last term on the RHS of Eq. (8) is the Darcy-Forchheimer term for pressure loss due to flow through the porous material, with the linear and turbulent permeability coefficients k_1 and k_2, respectively. d_{disp} is the characteristic dispersion length and η the tortuosity. The diffusive fluxes are computed as:

$$\vec{j}_k = -\rho\left(\frac{D_{m,k}^{\mathrm{mole}}}{\eta} + 0.5|\vec{u}|d_{\mathrm{disp}}\right)\nabla Y_k - Y_k\rho\frac{D_{m,k}^{\mathrm{mole}}}{\bar{M}\eta}\nabla\bar{M} \tag{12}$$

where $\bar{M}$ is the mean molar mass of the mixture, and the diffusion coefficient is

$$D_{m,k}^{\mathrm{mole}} = \frac{1-Y_k}{\sum_{j\neq k}\frac{X_j}{\mathcal{D}_{j,k}}} \tag{13}$$

where X_j is the mole fraction and $\mathcal{D}_{j,k}$ the binary diffusion coefficient. The energy equation for the solid phase reads

$$(1-\gamma)\rho_s c_s\beta\frac{\partial T_s}{\partial t} = \nabla\cdot(\lambda_{s,\mathrm{eff}}\nabla T_s) + \nabla\cdot(\lambda_{\mathrm{rad}}\nabla T_s) + h_v(T-T_s) \tag{14}$$

where c_s is the heat capacity of the solid and the numerical coefficient β accelerates the convergence to the steady state. The heat conductivity of the solid phase is $\lambda_{s,\mathrm{tot}} = \lambda_{s,\mathrm{eff}} + \lambda_{\mathrm{rad}}$, where $\lambda_{s,\mathrm{eff}}$ is the effective thermal conductivity of the solid and λ_{rad} models radiative heat transfer using the Rosseland model [27] as $\lambda_{\mathrm{rad}} = 16\sigma T_s^3/(3\kappa)$, with the Stefan-Boltzmann constant σ and the extinction coefficient κ.

Effective material properties

For closing the VAS governing equations written above, effective material properties are calculated from the µ-CT scans and finite-volume simulations performed using the open-source code PUMA [28]. Background noise in the µ-CT scans is reduced using a 3D Gaussian filter and the threshold values for segmentation into gas and solid phases are calculated using the Otsu method [29]. The material properties

Table 2. Material properties

Property	value
γ (%)	72.9
d_p (mm)	2.85
S_v (m^{-1})	891
η (mm^{-1})	1.48
a ($Wm^{-1}K^{-1}$)	10.4
b (-)	-0.53
κ (m^{-1})	650

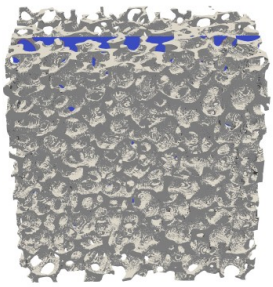

Figure 2. μ-CT scan of 15 PPI ceramic foam

of the 15 PPI ceramic foam are given in Tab. 2. The coefficients $\lambda_{s,\text{eff}}$ and h_v are calculated using the expressions

$$\lambda_{s,eff} = a\left(\frac{T_s}{T_0}\right)^b, \qquad h_v = Nu\frac{S_v\lambda}{d_h} \tag{15}$$

where $T_0 = 293$ K, $d_h = 4\gamma/S_v$ is the hydraulic diameter of the porous medium, S_v the specific surface area, and $Nu = 3.7Re^{0.38}Pr^{0.25}$ is the Nusselt number. The coefficients a and b are given in Tab. 2 and the Reynolds Re and Prandtl Pr numbers are defined as

$$Re = \frac{\rho|\vec{u}|d_h}{\mu}, \qquad Pr = \frac{c_p\mu}{\lambda}. \tag{16}$$

The characteristic dispersion length d_{disp} is defined as a function of geometric properties and taken to be $d_{\text{disp}} = 10d_p$ in the present work.

Computational setup

The 2D computational domain used for the VAS is shown in Fig. 3. The channels are 25 mm long and followed by 25 mm of porous zone. The widths of the middle and side channels are 1 mm and 0.5 mm, respectively. Cyclic boundary conditions are applied on the burner sides. The boundary conditions

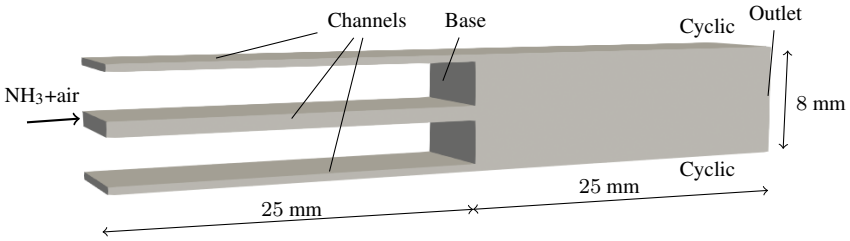

Figure 3. Computational domain used for VAS

at the inlet and channel walls are set in line with the DPLS. The outlet of the gas phase is adiabatic, and a radiation boundary condition towards the ambient temperature is set for the solid phase outlet. Pure gas phase is considered in the channels where the porosity is set to unity. Different from the DPLS, a pure gas phase section downstream of the porous zone can be omitted in the VAS. The cell size in the porous zone is 4×10^{-5} m and the computational domain has a total of 67,000 cells. The spatial derivatives are calculated using second-order central differences, and a first-order Euler scheme is used for time integration. The maximum CFL number is set to 0.5 for the transient simulations. Each VAS case is parallelised to a maximum of 96 cores and requires $\approx$ 2,400 CPU-h to achieve a steady state.

Results and discussion

Volume-averaged simulations

VAS of NH_3/air combustion are performed for a burner surface load of 0.25 MW/m^2. Operating conditions are defined using equivalence ratios between 0.8 and 1.2. Based on the full set of VAS results

(omitted here for brevity) equivalence ratios between $\phi = 0.9$ and $\phi = 1.1$ lead to low NO_x emissions and limited NH_3 slip. For our first pore-resolved investigation, DPLS are performed at $\phi = 0.9$. The VAS temperature profiles along the burner axis for $\phi = 0.9$ are shown in Fig. 4. The solid temperature profile T_s from the VAS is implemented as the solid boundary condition for the gas phase in the DPLS.

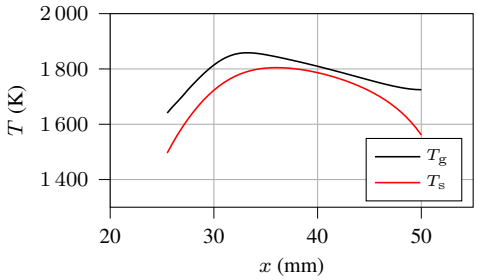

Figure 4. Axial solid and gas temperature profiles calculated by VAS of NH_3/air combustion at $\phi = 0.9$

Direct pore-resolved simulations

Flame propagation

The propagation of the flame over time is visualised through the OH mass fraction field and gas temperature in Fig. 5, where the white space represents the solid matrix. The gas temperature boundary condition derived from the VAS, see Fig. 5 (top), has a noticeable effect on the ignition and propagation of the flame front within the solid matrix. Note that in Fig. 5 we define a shifted x-coordinate x' that has its origin at the base of the porous burner matrix. The DPLS is initialised with a NH_3/air mixture at $\phi = 0.9$ in the channels and hot air inside the burner. The flame ignites at $x = 35$ mm ($x' = 10$ mm), which corresponds to the location of the peak temperature at the ceramic foam surface. After ignition, the flame front first moves upstream towards the inlet mixture and then slightly downstream, stabilising itself after $t = 20$ ms on the solid struts as illustrated in Fig. 5.

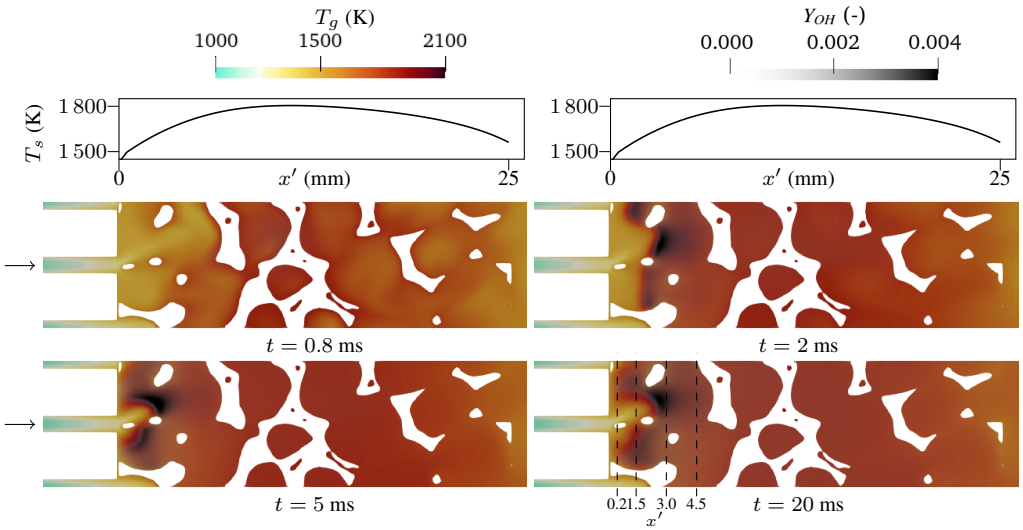

Figure 5. Flame propagation within the solid matrix from $t = 1$ to $t = 20$ ms shown in a $x - y$ sectional plane through the middle of the burner. The solid temperature boundary condition for the DPLS extracted from the VAS is plotted at the top.

Flame structure

The flame is stabilised near the channel outlets as shown in Fig. 6. To track the combustion process, a reaction progress variable is defined as

$$c = \frac{Y_{H_2O}}{Y_{H_2O,\text{burnt}}}. \tag{17}$$

The 3D structure of the flame is shown as iso-surfaces of the progress variable in Fig. 6 (left). It can be observed that the flame structure is composed of individual laminar flames over each channel outlet, where the struts of the solid matrix act as flame anchors. The solid matrix combined with the velocity profiles at the channel outlet define the local extent of the reaction zone. The maximum penetration of

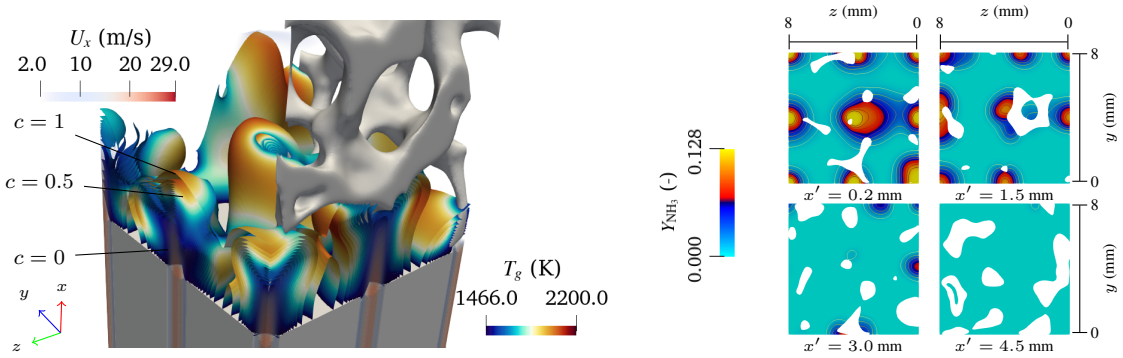

Figure 6. Left: 3D structure of the flame shown by iso-surfaces of progress variable c, coloured by gas temperature. Flow in the channels is visualised through the axial velocity component. Right: Cross-sections of the burner along the x-axis as indicated by the dashed vertical lines in Fig. 5 (right), with Y_{NH_3} illustrating the penetration of the fresh gases into the solid matrix.

unburnt fuel ($x' = 4.5$ mm) is observed above the side channels, where the channel outlet can be free or partially blocked by a strut as shown in Fig. 6 (right). The flame reaches the next solid strut in the flow direction. A strut partially blocks the central channel outlet and the flame wraps itself around the strut, stretching to $x' = 3.1$ mm. Comparatively lower fuel penetration is observed above the corner channels. Along with the accelerating flow and local porosity within the solid matrix, the foam surface temperature also affects flame stabilisation. The base temperature is 1430 K, which is above the auto-ignition temperature of NH_3/air. At $x' = 5$ mm, the foam surface temperature is above 1700 K, see Fig. 5 (top). The high surface temperature makes the upstream struts anchoring points for the flame and restricts further flame penetration within the solid matrix. High temperatures also promote the dehydrogenation of NH_3 as discussed next.

Ammonia dehydrogenation

Partial conversion of NH_3 into H_2 can potentially enhance NH_3 combustion by increasing the flame speed [30]. Gas temperatures in the reaction zone are high enough to achieve 99% conversion efficiency. Mass fraction and reaction rate of hydrogen in a 2D plane at $z = 4$ mm are shown in Fig. 7 (left). Iso-lines of the progress variable are plotted over the H_2 mass fraction and the peak Y_{H_2} is observed between $c = 0.6$ and $c = 1.0$. The ammonia conversion ratio [31] is calculated as $\mathcal{C} = 2X_{H_2}/(2X_{H_2} + 3X_{NH_3})$, where X_i is the mole fraction of species i. For maximum $\dot{\omega}_{H_2}$, the ammonia conversion ratio is 0.275. The progress variable is plotted as contour lines in the reaction zone as shown in Fig. 7 (left). To track

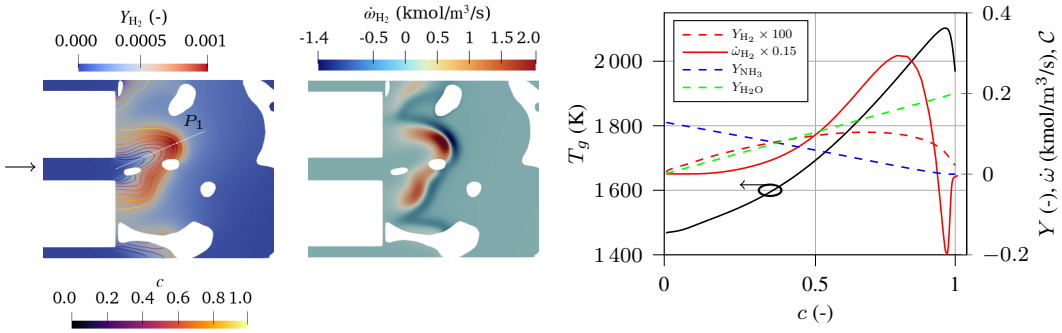

Figure 7. Left: Ammonia dehydrogenation as visualised through the mass fraction and reaction rate of H_2 shown in a 2D plane in the middle of the burner. Iso-lines show the progress variable in the reaction zone. Right: Species and gas temperature profiles along the line P_1 shown on the left plotted against reaction progress variable.

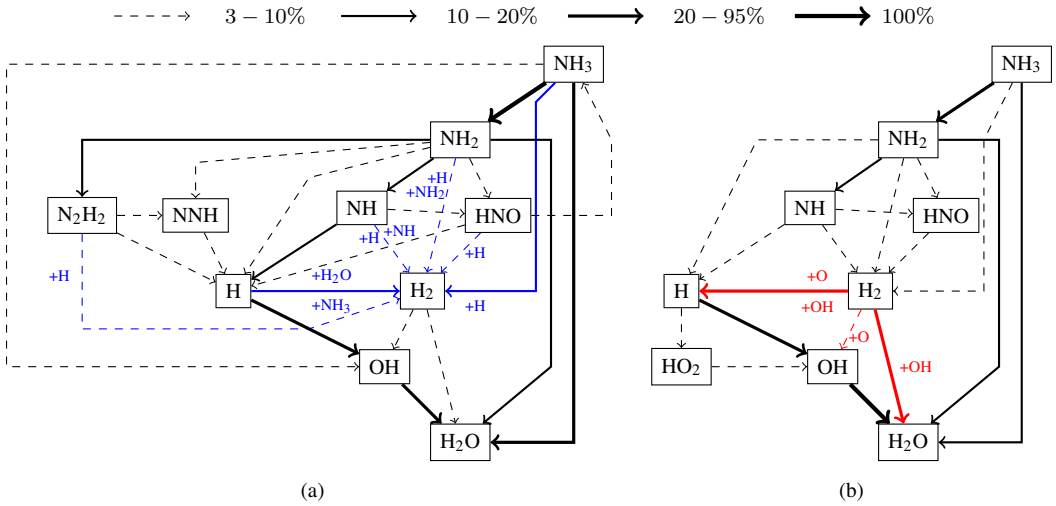

Figure 8. Reaction path diagrams for the location of the maximum (a) production and (b) consumption rate of H_2

intermediate hydrogen production in the reaction zone, major species mass fractions, gas temperature and the H_2 reaction rate are plotted along the line P_1 from Fig. 7 (left) as a function of c in Fig. 7 (right). Compared to Y_{NH_3}, Y_{H_2} is relatively small in the reacting mixture. The production rate of H_2 increases with T_g until $c = 0.7$ and falls sharply towards the burnt gases. The highest consumption rate of H_2 is at $c = 0.93$, which coincides with peak T_g. Thus, for the largest part of the reaction zone, combustion is driven by NH_3 with little production of H_2, but switches to H_2 near the burnt gases.

The reaction pathways for the locations of maximum H_2 production and consumption rates are shown in Fig. 8. The path diagrams are generated by following the H atom and the reaction fluxes are normalised with the maximum flux in the diagram. The reaction paths that directly contribute to H_2 production are shown in blue in Fig. 8 (left). The most important reaction pathways (blue solid arrows) leading to H_2 production are

$$NH_3 + H \longrightarrow H_2 + NH_2 \tag{18}$$

$$H + H_2O \longrightarrow H_2 + OH. \tag{19}$$

The direct contribution of H_2 to H_2O product formation is negligible (4.7%) compared to NH_3, where the H-abstraction reactions and direct conversion of NH_3 are the primary pathways to H_2O. Solid red arrows in Fig. 8 (right) are the primary reactions responsible for the consumption of H_2.

$$H_2 + OH \longrightarrow H + H_2O \tag{20}$$

The presence of a distinct H_2 flame highlights the dehydrogenation process in NH_3 combustion, but its contribution to the overall combustion process is very low.

DPLS vs. VAS

In this section, the VAS results are compared to equivalent volume-averaged results extracted from the DPLS. Volume-averaging of the DPLS data is performed by considering different axial lengths l_{RV} of the reference volume and comparing the axial profiles. Minimal variation is observed in the axial profiles for 31 µm $< l_{RV} <$ 125 µm and $l_{RV} = 62$ µm is used for the volume-averaging of the DPLS data. Figure 9 shows a quantitative comparison of the axial profiles between VAS and DPLS.

Due to the effects of local flow acceleration and high foam surface temperatures, the DPLS flame stabilises near the channel outlets. The reduced-order VAS approach leads to discrepancies with the volume-averaged DPLS, particularly near the outlet of the channels and in the reaction zone. A double peak is observed in the DPLS profile of T_g. The first peak corresponds to the heat released in the reaction zone. The higher foam surface temperature downstream of the reaction zone re-heats the products, resulting in the second peak of T_g, which is attributed to the simplified (fixed) temperature BC in the

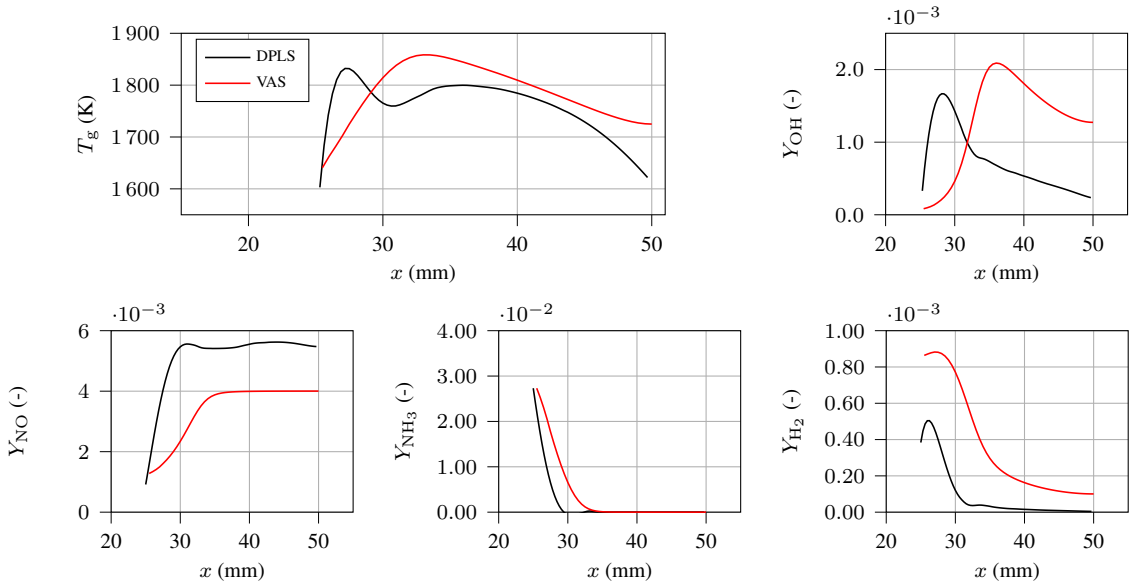

Figure 9. Comparison of axial species and gas temperature profiles between the DPLS and VAS

DPLS. The VAS model does not consider the local stretching/shrinking of the flame front as well as localised flame-solid interactions. Geometric properties of the ceramic foam assumed to be uniform in VAS can have a spatial variation that is represented in DPLS. In spite of this, the difference in peak T_g is only 30 K. The species profiles in Fig. 9 confirm the more upstream flame stabilisation in the DPLS and show comparable orders of magnitude between DPLS and VAS. The discrepancies could be attributed to the variable porosity of the 15 PPI foam scanned for the DPLS, where γ varies from 0.91 to 0.76 for $x' = 0.2...5$ mm. The constant porosity assumption in VAS leads to higher inter-phase heat transfer and ammonia dehydrogenation downstream of the flame front. On the other hand, the peak Y_{H_2} in DPLS is close to the flame front. At the respective flame fronts, both VAS and DPLS show comparable Y_{H_2}. Moreover, there is a hydrogen slip observed in VAS, which could explain the lower Y_{NO}.

Conclusions

PMC of premixed NH_3/air was investigated by means of DPLS and VAS. VAS were performed for a 15 PPI foam at various burner operating conditions to find optimal conditions for limited NO_x emissions and negligible NH_3 slip. DPLS were performed for a lean fuel condition at $\phi = 0.9$ to analyse the combustion process within the solid matrix in more detail. However, the solid temperature predicted by the VAS was implemented as the foam surface temperature in the DPLS. The unburnt gas mixture auto-ignited when in contact with the foam surface at peak temperature. The flame front moved upstream and stabilised itself near the base of the porous matrix. Maximum penetration of unburnt fuel within the solid matrix was affected by local flow acceleration, high foam surface temperature, and the foam geometry. Ammonia dehydrogenation led to a production of H_2 which assisted the stabilisation of the NH_3 flame. A distinct H_2 flame was observed, where combustion between $c = 0.93$ and $c = 1.0$ was primarily driven by H_2 produced in the upstream reaction zone. Volume-averaged temperature and species profiles from the DPLS were compared with the VAS results. Clear discrepancies were attributed to the missing consideration of flame-solid interaction and spatial variation of geometric properties in the VAS and a fixed foam surface temperature in the DPLS. Further investigation of NH_3/air PMC at various operating conditions and in different porous geometries will be performed in future works.

Acknowledgements

The authors acknowledge the financial support by DFG, Germany (project number: 523876164, within PP2419 HyCAM) and the Helmholtz Association of German Research Centers (HGF), within the research field Energy, program Materials and Technologies for the Energy Transition (MTET), topic Re-

source and Energy Efficiency. The authors gratefully acknowledge the Gauss Centre for Supercomputing e.V. for providing computing time through the John von Neumann Institute for Computing (NIC) on the GCS Supercomputer JURECA at Jülich Supercomputing Centre (JSC). We also acknowledge the support of Jana Hubálková from TU Freiberg, who performed the original μ-CT scans of the 15PPI foams.

References

[1] Pitsch H., Proc. Combust. Inst. 40 (1) (2024) 105638.
[2] Hossain Bhuiyan M. M., Siddique Z., International J. Hydr. Energy 102 (2025) 1026–1044.
[3] Lucentini I., Garcia X., Vendrell X., Llorca J., Industrial and Engineering Chemistry Research 60 (51) 18560–18611.
[4] Aziz M., Wijayanta A. T., Nandiyanto A. B. D., Energies 13 (12) (2020) 3062.
[5] Murai R., Nakatsuka N., Higashino H., Akamatsu F., Springer Nature Singapore, Singapore, 2023, pp. 627–640, CO_2 Free Ammonia as an Energy Carrier: Japan's Insights.
[6] Elbaz A. M., Wang S., Guiberti T. F., Roberts W. L., Fuel Communications 10 (2022) 100053.
[7] Kobayashi H., Hayakawa A., Somarathne K. K. A., Okafor E. C., Proc. Combust. Inst. 37 (1) (2019) 109–133.
[8] Trimis D., Durst F., Combustion Science and Technology 121 (1-6) (1996) 153–168.
[9] Guillaume V., Bassem A., Edna R. T., Emeric B., Matthias I., Proc. Combust. Inst. 39 (4) (2023) 4195–4204.
[10] Barra A. J., Diepvens G., Ellzey J. L., Henneke M. R., Combust. Flame 134 (4) (2003) 369–379.
[11] Ferguson J. C., Sobhani S., Ihme M., Proc. Combust. Inst. 38 (2) (2021) 2127–2134.
[12] Boigné E., Zirwes T., Parkinson D. Y., Vignat G., Muhunthan P., Barnard H. S., MacDowell A. A., Ihme M., Combust. Flame 259 (2024) 113132.
[13] Bedoya C., Dinkov I., Habisreuther P., Zarzalis N., Bockhorn H., Parthasarathy P., Combust. Flame 162 (10) (2015) 3740–3754.
[14] Liu Y., Deng Y., Shi J., Xiao R., Li H., Chinese Journal of Chemical Engineering 34 (2021) 87–96.
[15] Wieland C., Weis C., Habisreuther P., Trimis D., Combust. Flame 245 (2022) 112370.
[16] Muller F., Dounia O., Selle L., Physics of Fluids 36 (1) (2024) 013336.
[17] Mishra S., Steven M., Nemoda S., Talukdar P., Trimis D., Durst F., Int. Comm. Heat and Mass Trans. 33 (4) (2006) 467–474.
[18] Bidi M., Nobari M., Avval M. S., Energy 35 (8) (2010) 3483–3500.
[19] Sahraoui M., Kaviany M., Int. Journ. Heat and Mass Tran. 37 (18) (1994) 2817–2834.
[20] Masset P.-A., Duchaine F., Pestre A., Selle L., Combust. Flame 251 (2023) 112678.
[21] Zirwes T., Vignat G., Toro E. R., Boigné E., Younes K., Trimis D., Ihme M., Combust. Flame 257 (2023) 113020.
[22] Goodwin D. G., Moffat H. K., Schoegl I., Speth R. L., Weber B. W., Cantera: An Object-oriented Software Toolkit for Chemical Kinetics, Thermodynamics, and Transport Processes, V3.0.0 (2023).
[23] Zirwes T., Sontheimer M., Zhang F., Abdelsamie A., Pérez F. E. H., Stein O. T., Im H. G., Kronenburg A., Bockhorn H., Flow, Turb. Combust. 111 (2) (2023) 567–602.
[24] Kee R. J., Coltrin M. E., Glarborg P., Zhu H., Chemically Reacting Flow, Molecular Transport (2017) 371–416, John Wiley & Sons, Ltd.
[25] Hindmarsh A. C., Brown P. N., Grant K. E., Lee S. L., Serban R., Shumaker D. E., Woodward C. S., ACM Transactions on Mathematical Software (TOMS) 31 (3) (2005) 363–396.
[26] Stagni A., Cavallotti C., Arunthanayothin S., Song Y., Herbinet O., Battin-Leclerc F., Faravelli T., React. Chem. Eng. 5 (2020) 696–711.
[27] Brenner G., Pickenäcker K., Pickenäcker O., Trimis D., Wawrzinek K., Weber T., Combust. Flame 123 (1) (2000) 201–213.
[28] Ferguson J. C., Semeraro F., Thornton J. M., Panerai F., Borner A., Mansour N. N., SoftwareX 15 (2021) 100775.
[29] Otsu N., IEEE Trans. Sys., Man, and Cyber. 9 (1) (1979) 62–66.
[30] Nozari H., Karabeyoğlu A., Fuel 159 (2015) 223–233.
[31] Mei B., Zhang J., Shi X., Xi Z., Li Y., Combust. Flame 231 (2021) 111472.